

RESOLVED STRUCTURE OF ARP 220 NUCLEI AT $\lambda \approx 3$ MM

KAZUSHI SAKAMOTO,¹ SUSANNE AALTO,² LORETO BARCOS-MUÑOZ,^{3,4} FRANCESCO COSTAGLIOLA,² AARON S. EVANS,^{5,4}
NANASE HARADA,¹ SERGIO MARTÍN,^{3,6} MARTINA WIEDNER,⁷ AND DAVID WILNER⁸

¹*Academia Sinica, Institute of Astronomy and Astrophysics, Taipei 10617, Taiwan*

²*Department of Earth and Space Sciences, Chalmers University of Technology, Onsala Observatory, 439 92 Onsala, Sweden*

³*Joint ALMA Observatory, Alonso de Córdova 3107, Vitacura, Santiago, Chile*

⁴*National Radio Astronomy Observatory, 520 Edgemont Road, Charlottesville, VA 22903, USA*

⁵*Department of Astronomy, University of Virginia, P.O. Box 400325, Charlottesville, VA 22904, USA*

⁶*European Southern Observatory, Alonso de Córdova 3107, Vitacura, Santiago, Chile*

⁷*LERMA, Observatoire de Paris, PSL Research University, CNRS, Sorbonne Universités, UPMC Univ. Paris 06, F-75014 Paris, France*

⁸*Harvard-Smithsonian Center for Astrophysics, 60 Garden Street, Cambridge, MA 02138, USA*

(Accepted for publication in ApJ)

ABSTRACT

We analyze 3 mm emission of the ultraluminous infrared galaxy Arp 220 for spatially-resolved structure and spectral properties of the merger nuclei. ALMA archival data at $\sim 0''.05$ resolution are used for extensive visibility fitting and deep imaging of continuum emission. The data are fitted well with two concentric components for each nucleus, such as two Gaussians or one Gaussian plus one exponential disk. The larger components in individual nuclei are similar in shape and extent, ~ 100 – 150 pc, to the cm-wave emission due to supernovae. They are therefore identified with the known starburst nuclear disks. The smaller components in both nuclei have about a few 10 pc sizes and peak brightness temperatures (T_b) more than twice higher than in previous single-Gaussian fitting. They correspond to the dust emission that we find centrally concentrated in both nuclei by subtracting the plasma emission measured at 33 GHz. The dust emission in the western nucleus is found to have a peak $T_b \approx 530$ K and a full width at half maximum of about 20 pc. This component is estimated to have a bolometric luminosity on the order of $10^{12.5} L_\odot$ and a 20 pc-scale luminosity surface density $10^{15.5} L_\odot \text{kpc}^{-2}$. A luminous AGN is a plausible energy source for these high values while other explanations remain to be explored. Our continuum image also reveals a third structural component of the western nucleus — a pair of faint spurs perpendicular to the disk major axis. We attribute it to a bipolar outflow from the highly inclined ($i \approx 60^\circ$) western nuclear disk.

Keywords: galaxies: active — galaxies: individual (Arp 220) — galaxies: ISM — galaxies: nuclei

1. INTRODUCTION

The nearest ultraluminous infrared galaxy Arp 220 has been a key object in our study of the luminous phase in galaxy evolution after a major merger (Sanders & Mirabel 1996; Hopkins et al. 2008). It has two merger nuclei separated by about $1''$ (~ 400 pc) on the sky (Scoville et al. 1998; Genzel et al. 2001) each having a ~ 100 pc scale rotating disks of molecular gas (Sakamoto et al. 1999). Vigorous star formation is evident in the nuclei from radio emission due to supernovae (Smith et al. 1998; Barcos-Muñoz et al. 2015, hereafter BM15). Molecular outflows from the individual nuclei have been found (Sakamoto et al. 2009) as is often the case for luminous galactic nuclei (e.g., Ciccone et al. 2014; Sakamoto et al. 2014). Arp 220 is therefore undergoing merger-driven rapid evolution of galaxy nuclei. Important open issues about the galaxy include the gas flows to, from, and within the two merger nuclei and the structure, physical and chemical properties, and the dominant luminosity sources of the nuclei. On the last point, while nuclear starburst is evident whether there are any active galactic nuclei (AGN) with significant luminosities is still under intense study (Yoast-Hull et al. 2017; Paggi et al. 2017, and references therein) mainly because the nuclei are extremely obscured ($N_{\text{H}} \geq 10^{25-26} \text{ cm}^{-2}$, Sakamoto et al. 2008; Wilson et al. 2014; Martín et al. 2016; Scoville et al. 2017, hereafter S17). High-resolution observations at centimeter to sub-millimeter wavelengths are especially useful for many of the open issues thanks to the lower opacity compared to shorter wavelengths.

We recently found from our 1 and 0.8 mm observations of Arp 220 with the Atacama Large Millimeter-submillimeter Array (ALMA) that individual merger nuclei have composite structure (Sakamoto et al. in prep.). Each nucleus consists of a central compact core and a more extended structure that can be together fitted with two Gaussians. The single Gaussian models that had been used before are not adequate anymore for high quality data at $\lesssim 0''.2$ resolution. The central core components have sizes as small as $0''.1$ – $0''.05$ in full width at half maximum (FWHM) and have higher peak brightness temperatures than estimated with single-Gaussian fits. They are of great interest for unveiling the unknown nature of the luminosity source and to trace the evolution of the merger nuclei. We have therefore extended our structural analysis of the Arp 220 nuclei to ALMA archival data obtained at around 3 mm at $\sim 0''.05$ resolution. We have also decomposed the 3 mm continuum to plasma and dust emission and mapped the dust emission in individual nuclei. This paper reports the results.

We will refer to the eastern nucleus of Arp 220 as Arp 220 E (sometimes just ‘E’ for short) and the western nucleus as Arp 220 W (or just W). All features within about $0''.5$ of the centroid of each nucleus will be referred to in this way. We adopt an angular size distance of $D_{\text{A}} = 85.0$ Mpc ($1'' = 412$ pc), luminosity distance $D_{\text{L}} = 87.9$ Mpc, and the total IR luminosity of $L_{8-1000 \mu\text{m}} = 10^{12.28} L_{\odot}$ for the galaxy (Armus et al. 2009) to be consistent with S17.

2. ALMA DATA

We analyzed archival data of the ALMA project 2015.1.00113.S (P.I. Scoville). S17 already reported a part of the project regarding $^{12}\text{CO}(1-0)$ and continuum imaging as well as spatial and spectral modeling of the CO emission. The dataset consists of two tunings around 100 GHz consecutively observed on 2015 Oct. 27 in a long-baseline configuration; S17 analyzed the one with CO. Both used J1550+0527 for flux and bandpass calibration. We adopted for it a flux model $(S_{\nu}/\text{Jy}) = 1.000 \times (\nu/104.0 \text{ GHz})^{-0.602}$ that is from the nearest records in the ALMA Calibrator Source Catalogue, i.e., four measurements made at 91.5 and 233 GHz on Oct. 31 and Nov. 1.¹ We flagged three poorly performing antennas, DA45, DA65, and DV20, and used the remaining 37. The projected baseline lengths for Arp 220 ranged 0.24–10.38 km for the first tuning with ^{12}CO and 0.22–11.10 km for the second with ^{13}CO . We used CASA 4.7.2 for our data reduction (McMullin et al. 2007), starting from the raw data and following the steps of the observatory-provided calibration except the revised calibrator flux model and the additional flagging of DA65 and DV20. We made phase-only self calibration using continuum. It was first done independently for the two tunings, and we used that data for our visibility fitting. Another round was made after combining the two datasets and before making the images presented in this paper.

¹ The ALMA Observatory used the Morita Array (7m array) for the quasar measurements, tied them to the measurements of Neptune, Mars, and Titan on the same days, and used the Butler-JPL-Horizons 2012 model for the solar system objects. The expected flux calibration accuracies in the ALMA Cycle 3 Proposer’s Guide are (better than) 5% and 10% for 92 GHz and 233 GHz, respectively. For our calibrator, two measurements at each frequency agree quite well. As a result the formal 1σ uncertainties of our calibrator model are 0.004 Jy for the flux density and 0.10 for the spectral index after normalizing the power-law fit uncertainties so that the reduced χ^2 is unity. These uncertainties do not include any error due to deviation of the quasar spectral energy distribution from a power-law and model uncertainties of the solar system objects. The Observatory used for the archived data products $(S_{\nu}/\text{Jy}) = 1.126 \times (\nu/104.0 \text{ GHz})^{-0.680}$ for J1550+0527.

3. 3 MM SPECTRA OF THE TWO NUCLEI

Figure 1 shows the spectra sampled at individual nuclei with $0''.2$ and $0''.1$ beams. Major lines in the spectra are $^{12}\text{CO}(1-0)$, $\text{CN}(1-0)$ doublet, $\text{CH}_3\text{CN}(6-5)$, $\text{HC}_3\text{N}(12-11)$, $\text{HC}_3\text{N}(11-10)$, $\text{CS}(2-1)$, and $\text{C}^{34}\text{S}(2-1)$. The HC_3N lines include transitions within vibrationally excited states $v_7 = 1$ ($l = 1e$ and $1f$) and $v_7 = 2$. $^{13}\text{CO}(1-0)$ and $\text{C}^{18}\text{O}(1-0)$ are also in the frequency coverage but they are blended with other lines and inconspicuous. Other likely identifications are CH_3CCH and HC_5N while $\text{H}40\alpha$ is not detected. These lines and more have been detected in emission in single-dish observations by Aladro et al. (2015). In the ALMA high-resolution data here, the CN doublet is almost totally in absorption while $\text{CH}_3\text{CN}(6-5)$, $\text{CS}(2-1)$, $\text{C}^{34}\text{S}(2-1)$, and $\text{SO}(3_2-2_1)$ start to show absorption toward Arp 220 W at $0''.1$ resolution. While we will measure continuum source sizes later, this observation already indicates that the western nucleus has a bright continuum source or sources whose extent d satisfies $d \lesssim 0''.1$ and $d \ll 0''.1$, because lines would have been in absorption at both resolutions if $d \gtrsim 0''.2$ and in emission if $d \ll 0''.1$.

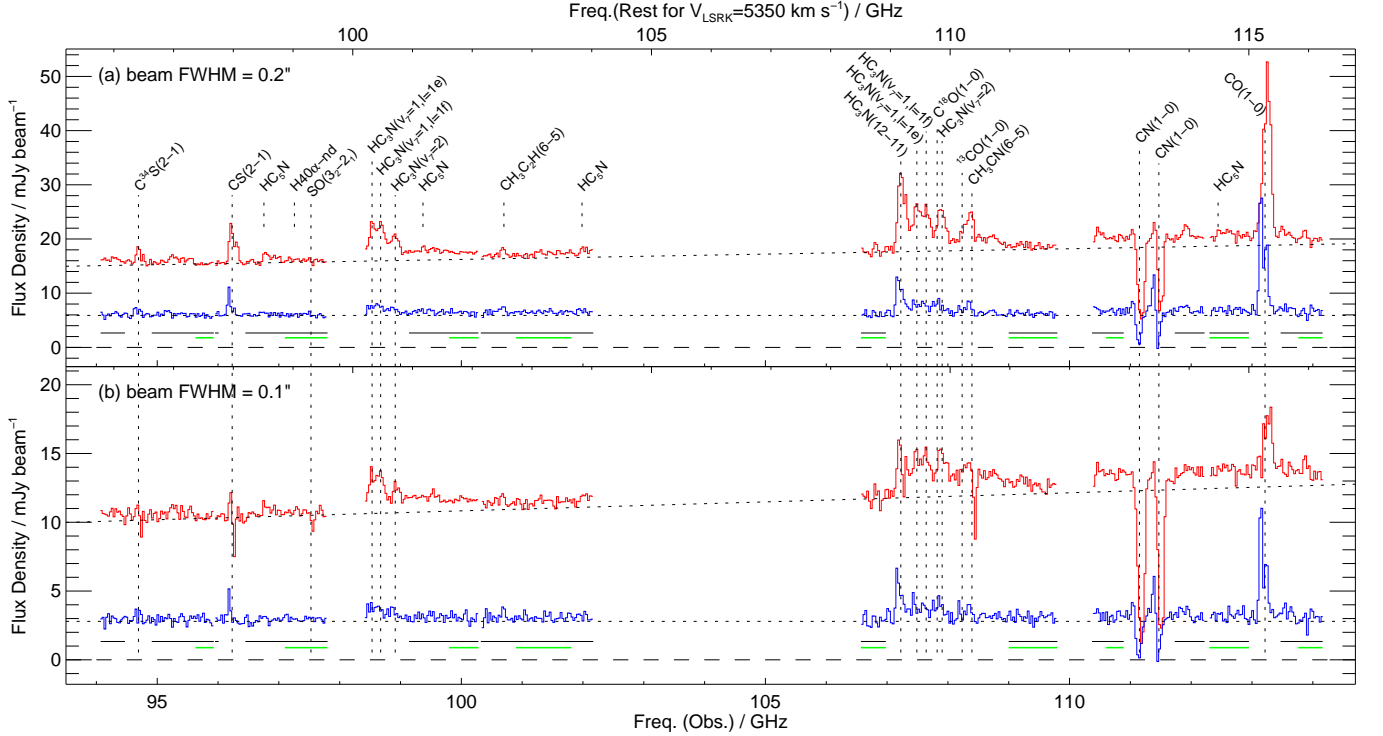


Figure 1. Spectra of Arp 220 nuclei around 100 GHz sampled at the western (red) and eastern (blue) nuclei. Data imaged at every 10 MHz were binned to 30 MHz and convolved from about $0''.09$ resolution to (a) $0''.2$ and (b) $0''.1$. Major lines are labeled with long vertical dotted lines. Some minor lines are also labeled with short vertical lines. Estimated power-law continuum is plotted for each nucleus as a black dotted line. Its power-law (i.e., spectral) index is $+1.2$ and 0.0 for the western and eastern nucleus, respectively, in both panels. Horizontal black and green bars below the spectra indicate the spectral segments that we analyzed as continuum-dominated channels. The black ones are used for continuum imaging and green for visibility fitting.

Continuum was first estimated by visually finding regions with least lines in each spectrum and fitting a power-law curve $S_\nu \propto \nu^\alpha$; off-line channels around 96–98, 107, and 109.5 GHz constrained the fit most. Obtained curves are plotted in Fig. 1 and have a power-law (i.e., spectral) indices $\alpha \equiv d \log S_\nu / d \log \nu$ of $+1.2$ for the western nucleus and 0.0 for the eastern nucleus with uncertainties about ± 0.2 . It is evident that the two nuclei have different spectral indices around 100 GHz. Arp 220 W has a positive index indicating significant contribution from thermal dust emission or partially opaque free-free emission. Arp 220 E has a nearly flat spectrum indicating much less contribution of such emission. Guided by these continuum fits and the observed spectra, we defined two sets of continuum-dominated channels (CDCs) for further analysis. The first (CDC₁) is marked with black horizontal bars in Fig. 1. They are more than 650 km s^{-1} from the systemic velocity for major lines but include weak possible lines such as HC_5N . The total bandwidth of CDC₁ is 9.5 GHz. Contribution of line emission to the integrated emission of CDC₁ is in the range of

5–10% for the two apertures and two nuclei. The second set of channels (CDC_2) is marked with green bars in Fig. 1. It is a subset of CDC_1 and avoids some weak lines.

4. VISIBILITY FITTING

We made model fitting of the calibrated visibilities to obtain continuum parameters of the two nuclei. Visibility fitting is a powerful way to analyze interferometric data when the target structure is simple and marginally resolved (e.g., Wiedner et al. 2002; Sakamoto et al. 2013).² For such cases, it is far more straightforward to fit visibilities than to make a dirty image first, deconvolve it next by iteratively finding clean components and convolving them with a clean beam, and then make image-domain deconvolution of the cleaned image. We made our non-linear visibility fitting in IDL using an implementation of the Levenberg-Marquardt algorithm called `mpfit` (Moré 1977; Moré & Wright 1993; Markwardt 2009).

4.1. 1G fit

We first fitted the visibilities using one Gaussian component for each nucleus; we call this the 1G fit. The whole data set was fitted in each and every 30 MHz channel. The resulting parameters, averaged in CDC_2 to minimize line contamination, are listed in Table 1. Our 1G-fit positions agree very well with those measured at 33 GHz by BM15. Our 1G-fit parameters are consistent with the deconvolved parameters of S17 for Arp 220 E but we obtained a smaller size ($0''.084 \times 0''.065$) and higher peak brightness temperature (386 K) for the more compact Arp 220 W, for which S17 obtained $0''.12 \times 0''.11$ for the deconvolved FWHM and 167 K for the peak deconvolved T_b . Our visibility-fit size agrees with our image-domain deconvolved size from a $0''.07$ resolution image made with `robust=0.5`.

4.2. r2G fit

We next fitted each nucleus with restricted two Gaussians (r2G fit) to see if we need more than one component for each nucleus. Minimally generalizing the 1G model, the r2G model has for each nucleus two elliptical Gaussians sharing the same center, axial ratio, and position angle. The shared parameters are fixed to the ones from the 1G fit. This model naturally defines an elliptic coordinate for each nucleus to plot visibilities as a function of the elliptic radius in the same manner as often done for a single axisymmetric source. For each nucleus, we first subtract the other nucleus and shift the phase center to the target nucleus, then we vector average the visibilities in elliptical annuli and fit the real part of the visibilities. (In all the other fitting in this section, complex visibilities were simultaneously fitted for the two nuclei without such subtraction.) The subtraction helps to visualize the fit because otherwise the two nuclei make stripes of visibility amplitude and phase in the uv plane. Without radial symmetry, any radial visibility plot will be less informative and harder to compare with models. We made two iterations to allow a better nucleus subtraction. The subtracted models were first from the 1G fit and then from the r2G fit obtained in the previous iteration. Any subtraction residual causes visibility ripples of $0.2 \text{ M}\lambda$ spacing, which corresponds to $1''$. They tend to cancel out when averaged in an elliptical annulus larger than $0.2 \text{ M}\lambda$. Since the cancellation is incomplete in smaller annuli, baselines shorter than $0.2 \text{ M}\lambda$ were flagged to suppress any subtraction residuals. The fitting was made for each of the nine sections of CDC_2 . All resulted in fits similar to an example in Figure 2, visually confirming that a single Gaussian is a poor fit for each nucleus while two (restricted) Gaussians can fit the data much better.

This result agrees with our observation at ~ 250 and 350 GHz (Sakamoto et al. in prep.). It is also in line with the finding of BM15 that 33 GHz (9 mm) continuum emission of individual nuclei is better fitted (in the image domain) by an exponential disk than by a Gaussian, because an r2G model and an exponential disk share a central cusp and slow outer decline. On the other hand, at 3 mm , neither nucleus is fitted by a single elliptical exponential disk³ as nicely as it is by the r2G model, although the difference is relatively small for Arp 220 E (see Fig. 2).

² For example, a Gaussian source with 50 mas FWHM on the sky has a Gaussian-shape distribution of visibility amplitude centered at the origin of the uv plane, with the amplitude declining to 50% and 6% of the central value (= total flux) at the uv radii of 0.9 and $1.8 \text{ M}\lambda$, respectively. Our data coverage to about $3 \text{ M}\lambda$ is sufficient to determine the amplitude distribution in the uv domain and hence the source size in the image domain, provided that visibilities have sufficient signal-to-noise ratio. While our dataset has a beam size of about 50 mas with the uniform weighting of visibilities, even a smaller size can be measured from a precise amplitude-to-uv radius curve (Martí-Vidal et al. 2012).

³ An axisymmetric exponential disk with a scale length a ,

$$f(x, y) = e^{-\sqrt{x^2+y^2}/a},$$

has the Fourier transform

$$\int_{-\infty}^{\infty} \int_{-\infty}^{\infty} f(x, y) e^{-i2\pi(ux+vy)} dx dy = \frac{2\pi a^2}{[1 + 4\pi^2 a^2(u^2 + v^2)]^{3/2}}.$$

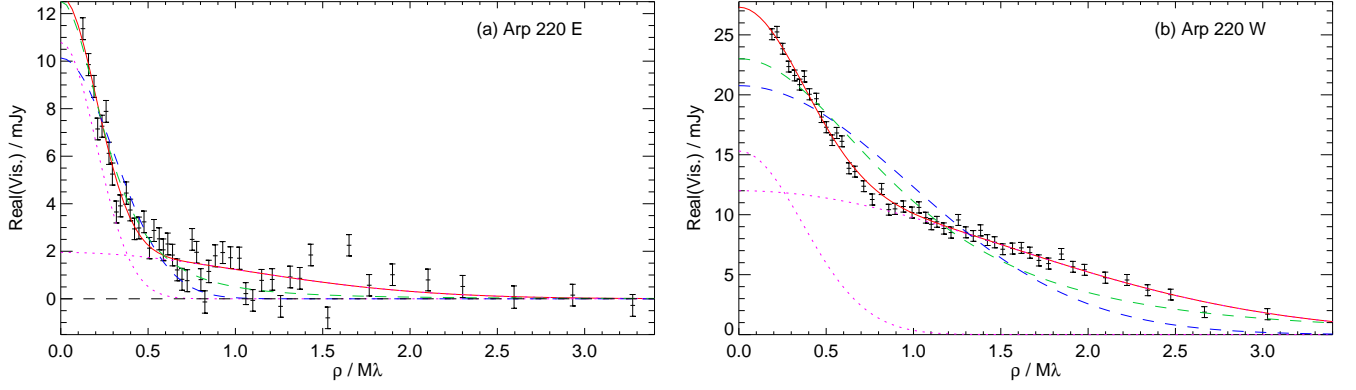


Figure 2. Arp 220 visibility fitting results for continuum-dominated channels around 112.6 GHz (a segment of CDC₂). Real part of visibilities are plotted as a function of the semi-minor axis of the elliptic coordinate in the u - v plane (see text for the fitting procedure). The data error bars are $\pm 1\sigma$. The magenta dotted curves are the two Gaussians whose sum, the red curve, best fits the data. The fitted major axis FWHM (θ_{maj}) at this frequency are the following. East nucleus: $\theta_{\text{maj}}^{(1)} = 74 \pm 16$ mas and $\theta_{\text{maj}}^{(2)} = 381 \pm 27$ mas. West nucleus: $\theta_{\text{maj}}^{(1)} = 50 \pm 1$ mas and $\theta_{\text{maj}}^{(2)} = 212 \pm 7$ mas. For comparison, the blue and green dashed curves show the best fits with a single Gaussian and an exponential disk, respectively.

4.3. 2G fit

After verifying that a single Gaussian provides a poor fit for each nucleus while two Gaussians can do much better, we fitted the continuum-dominated visibilities simultaneously using four Gaussians, two for each nucleus, without parameter restrictions (2G fit). Each Gaussian has six free parameters, one for total flux density, two for position, and three for shape. The fits easily converged with reduced χ^2 of 1.4–2.1. Figure 3 shows that the fitted parameters agree well among the nine CDC₂ segments even though they are from two observing sessions with independent calibration except for the common flux calibrator model. This assures that our spatial decomposition is robust and not limited to the r2G model. Table 1 lists averages of the derived parameters of individual components. Denoting the smaller component in each nucleus with a subscript 1 and the larger with 2, E₁ and W₁ have major axis FWHM of 88 mas (36 pc) and 50 mas (21 pc), respectively. Their peak brightness temperatures are as high as 73 K in E₁ and 640 K in W₁. They are more than twice smaller in size and warmer in brightness temperature than the single-Gaussian estimates in S17. The larger components E₂ and W₂ have major axis FWHM $0''.37$ and $0''.23$ (about 150, 100 pc) and peak brightness temperatures of 15 and 45 K, respectively. W₁ and W₂ have their major axes misaligned by about 50° while the eastern nucleus is reasonably fit with two Gaussians sharing virtually the same axial ratio and position angle. In each nucleus the compact and extended components are almost concentric with only 13–22 mas (5–9 pc) offsets between their centroids. It is noteworthy that the spectral index of W₁, 1.94 ± 0.16 , is consistent with that of the Rayleigh-Jeans part of optically thick emission, although the index can be instead due to a superposition of multiple kinds of emission with different spectral indices. The compact components E₁ and W₁ have about 20% and 47% of the 3 mm flux densities of the individual nuclei, respectively. Finally, we verified our 2G fitting by using data before any self-calibration. Sizes changed little and within the listed 1σ uncertainties. The largest change in peak T_b was only 5% reduction for W₁ to 607 ± 14 K.

4.4. 1G+1E fit

We made further fitting for parameters of dust emission in the nuclei. Plasma emission, i.e., synchrotron and free-free emission, dominates at 33 GHz and was fitted well in each nucleus as an exponential disk (BM15). We therefore employed two exponential disks having the parameters of the plasma disks (see Table 1), fractional contributions of the plasma and dust emission at 3 mm as we estimate in §6.2, and two Gaussians without fixed parameters. Each nucleus is therefore described as an exponential disk of fixed parameters plus a Gaussian (1G+1E fit). We refer to the Gaussian dust components in the two nuclei E₁' and W₁' and the plasma disks E₂' and W₂'. The employed flux contributions of dust emission are E₁'/E = 13% and W₁'/W = 41% at 3 mm. This 1G+1E fitting provided only an upper-limit size for the dust component in Arp 220 E but the limit is comparable to the size of E₁ in the 2G fit. Because E₁ has $\sim 20\%$ of the 3 mm flux density in the eastern nucleus while E₁' has 13%, we see that $E_1 \sim E_1'$. We obtained consistent results about Arp 220 W over the CDC₂ segments and the averaged parameters are in Table 1. The dust component

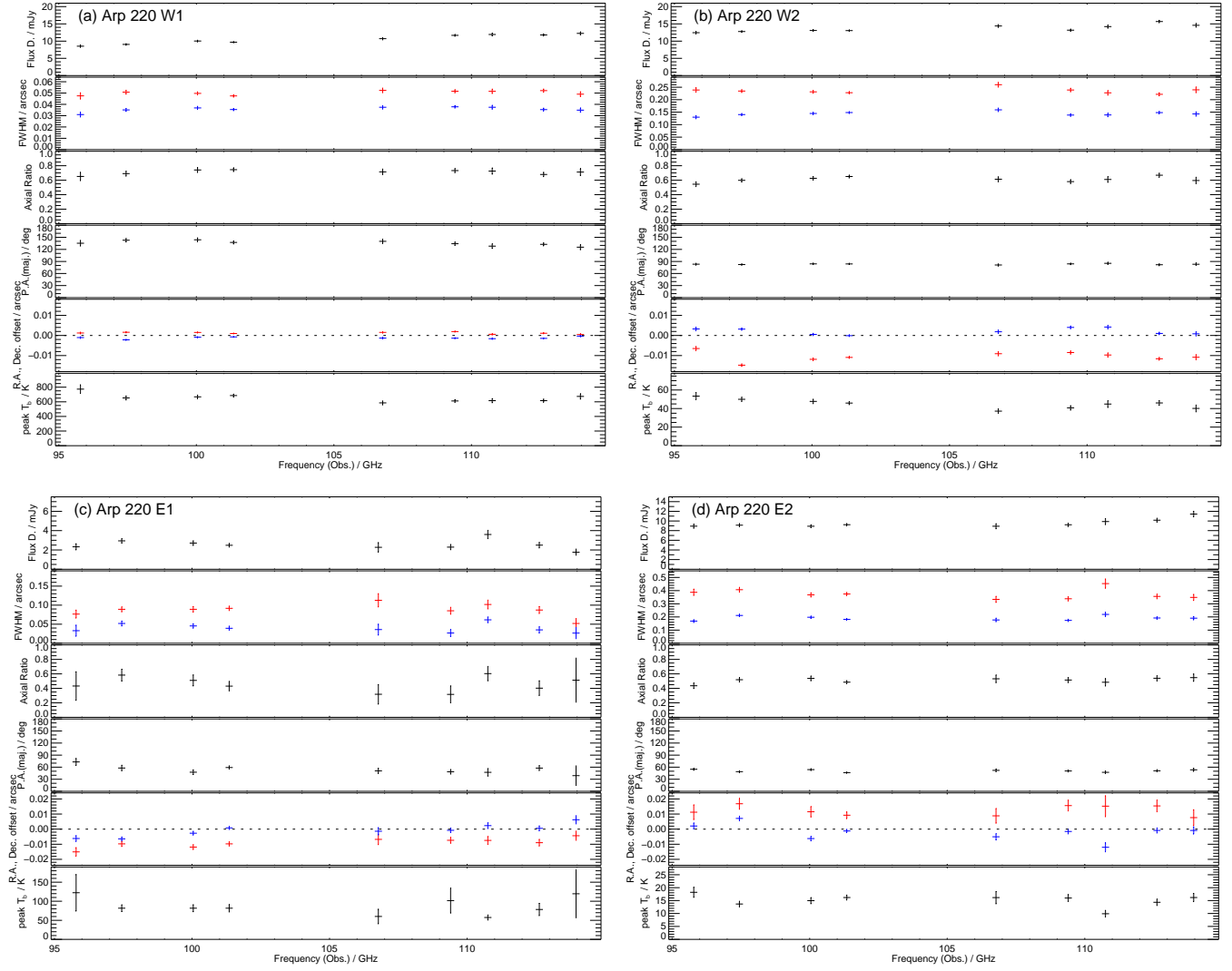


Figure 3. Arp 220 visibility fitting results for selected continuum-dominated channels (CDC_2). Visibilities were fitted with four elliptical Gaussians, two for each nucleus (2G fit). The six parameters of each Gaussian and two derived from them (axial ratio and peak brightness) are plotted. (a) and (b) are for the smaller and larger of the two Gaussians, respectively, to fit the west nucleus. (c) and (d) are for the east nucleus. The six sub-panels for each Gaussian show, from top to bottom, the source-integrated flux density, major (red) and minor (blue) axis FWHM, minor-to-major axial ratio, position angle of the major axis, positional offset (red for R.A. and blue for Dec.) from the 1G-fitting position of the nucleus, and peak Rayleigh-Jeans brightness temperature of the component. Error bars are $\pm 1\sigma$ and rescaled so that reduced χ^2 will be unity at each frequency.

W_1' has a spectral index 3.57 ± 0.21 as a direct consequence of our assumed spectral index of $\alpha_d = 3.8$ for the dust emission. Except for the spectral index, the parameters of W_1' are close to those of the component W_1 in our 2G fit including the flux density fraction of $W_1/W = 47\%$, hence $W_1 \approx W_1'$. Combining the results for the two nuclei, the compact components in our 2G fit represent mostly dust emission peaking at the centers of the two nuclei while the larger components in individual nuclei correspond to the exponential (circum)nuclear disks with dominant plasma emission. We are going to further discuss the decomposition in §6.

Table 1. Arp 220 Parameters from 3 mm Continuum

Parameter	Arp 220 E		Arp 220 W		unit
1 Gaussian fit					
major axis FWHM	227 ± 5	...	83.5 ± 1.2	...	mas
minor axis FWHM	111 ± 1	...	64.6 ± 1.1	...	mas
axial ratio (min./maj.)	0.453 ± 0.007	...	0.765 ± 0.010	...	
major axis P.A.	47.4 ± 1.0	...	110.4 ± 1.1	...	°
peak T_b	37.3 ± 1.4	...	385.5 ± 7.4	...	K
R.A.(ICRS) ^a 15 ^h 34 ^m	57.2917	...	57.2224	...	sec
Dec.(ICRS) ^a +23°30′	11.337	...	11.500	...	''
2 Gaussian fit					
component name	E ₁	E ₂	W ₁	W ₂	
major axis FWHM	87.9 ± 3.6	369 ± 9	50.0 ± 0.7	232 ± 3	mas
minor axis FWHM	43.5 ± 3.5	188 ± 5	36.0 ± 0.5	144 ± 2	mas
axial ratio (min./maj.)	0.471 ± 0.033	0.505 ± 0.011	0.717 ± 0.010	0.617 ± 0.012	
major axis P.A.	55.0 ± 2.4	49.8 ± 1.1	136.1 ± 1.9	83.3 ± 0.4	°
peak T_b	72.8 ± 4.6	14.7 ± 0.7	639.9 ± 13.7	45.0 ± 1.5	K
R.A. offset ^b	-9.6 ± 0.8	12.0 ± 1.1	1.3 ± 0.1	-11.1 ± 0.7	mas
Dec. offset ^b	-1.4 ± 1.2	-1.2 ± 1.5	-1.2 ± 0.2	1.6 ± 0.6	mas
spectral index α ^c	-0.96 ± 0.92	0.81 ± 0.29	1.94 ± 0.16	1.01 ± 0.25	
1Gaussian + 1Exp-disk fit ^d					
component name	E ₁ [']	E ₂ [']	W ₁ [']	W ₂ [']	
major axis size ^e	$\lesssim 70$	<i>82.1</i>	55.7 ± 1.3	<i>56.9</i>	mas
minor axis size ^e	$\lesssim 50$	<i>43.6</i>	32.9 ± 1.6	<i>33.9</i>	mas
axial ratio (min./maj.)	...	<i>0.531</i>	0.583 ± 0.020	<i>0.596</i>	
major axis P.A.	...	<i>54.7</i>	144.8 ± 1.9	<i>79.4</i>	°
peak T_b	529 ± 20	...	K
R.A. offset ^b	...	<i>0</i>	0.67 ± 0.16	<i>0</i>	mas
Dec. offset ^b	...	<i>0</i>	-0.97 ± 0.09	<i>0</i>	mas
spectral index α	...	<i>-0.59</i>	3.57 ± 0.21 ^f	<i>-0.61</i>	

NOTE— Parameters were obtained with visibility fitting. Fitting results from the nine segments of continuum-dominated channels (CDC₂) were averaged using the inverse square of their uncertainties as weights. Uncertainties of the means here are $\pm 1\sigma$ and do not include any systematic errors. The peak (Rayleigh-Jeans) brightness temperatures are subject to the flux calibration uncertainty on the order of 5% in this ALMA band.

^a Absolute astrometry is estimated to be accurate to 5 mas from the visibility fit positions of a test source J1532+2344 in the same observations.

^b Offset from the 1-Gaussian fit position.

^c Unaccounted errors due to low-level line contamination are expected for components with low brightness temperatures.

^d Parameters for the exponential disks E₂′ and W₂′, in italics, are from [BM15](#) and fixed.

^e Gaussian FWHM for E₁′ and W₁′ and exponential scale length for E₂′ and W₂′. For comparison between a Gaussian and an exponential disk, the half-light diameter of a Gaussian is its FWHM and that of an exponential disk is about 3.36 times the exponential scale length.

^f This spectral index is a consequence of an assumption about the spectral index of dust emission (§6.2). See §6.3 for a caution about the assumption.

5. IMAGES

We made continuum images from the continuum-dominated channels CDC_1 introduced in Section 3. Multi-frequency synthesis was made with two terms (i.e., the spectrum at each position is assumed to follow a power law) and using the robust weighting (Briggs 1995).

Figure 4 shows the 3 mm continuum images made with three different robust parameters. Dominant features in all are a bright compact source at the center of Arp 220 W (W_1 in our 2G fit) and larger elongated structures in the position angles of about 50° in E and 80° in W (E_2 and W_2 , respectively). Arp 220 E also has a compact central component (E_1) that is easier to see in the panel (c) with the highest resolution and equal-step contours at lower levels. The overall structure is consistent with our visibility fitting results. The peak intensities in the maps are lower than our fitted values as expected from beam dilution.

Looking for features that could not be captured with our simple models, we find in Fig. 4(a) that the western nucleus has faint bipolar features that extend from the central region along P.A. $\sim 170^\circ$ and perpendicular to the major axis of W_2 . This feature is below the lowest contour in the continuum image of S17, which corresponds to our third contour. The eastern nucleus also shows faint features in the panel (a) around the tips of its major axis, extending in the opposite directions like an integral sign. This is also seen at 33 GHz (BM15). In the panels (b) and (c), we see that the extended component E_2 starts to be resolved to multiple sources. This may be also the case for W_2 in the panel (c).

Fig. 4(b') compares the 3 mm continuum emission with the distribution of compact (< 2 pc) radio (18–2 cm) sources that were observed over 1994–2014 with VLBI (Varenius et al. 2017, and references therein). These sources have been almost entirely attributed to supernovae, i.e., radio supernovae and young supernova remnants (Smith et al. 1998; Lonsdale et al. 2006; Parra et al. 2007; Batejat et al. 2011; Varenius et al. 2017). The VLBI source distribution is similar to the 3 mm emission distribution in both nuclei, mainly following the larger E_2 and W_2 components. The similarity was also seen by BM15 with 33 GHz plasma emission at a comparable resolution of $0''.07$.

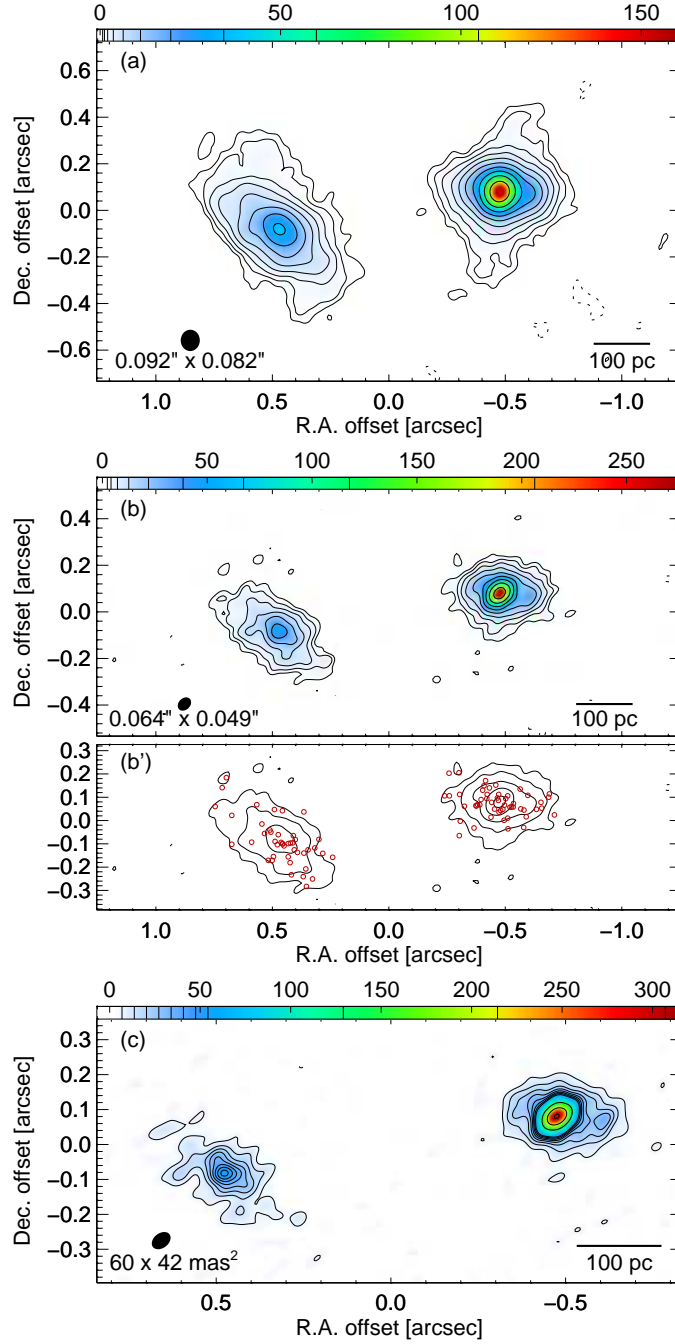


Figure 4. Arp 220 continuum images at 104.1 GHz (2.9 mm). Each panel has the FWHM beam size at the bottom-left corner. The offset coordinates are from the midpoint of the two nuclei. The intensity unit of the color bars is kelvin (Rayleigh-Jeans brightness temperature). (a) Imaged with `robust=2`, i.e., the natural weighting. The n -th contour is at $\pm 3n^{1.75}\sigma$ where $\sigma = 0.23$ K ($15 \mu\text{Jy beam}^{-1}$). The peak intensity is 161 K ($10.8 \text{ mJy beam}^{-1}$). Negative contours are dashed. (b) Imaged with `robust=0`. The n -th contour is at $\pm 3n^{1.75}\sigma$ where $\sigma = 0.78$ K. The peak intensity is 276 K. (b') The same image as (b) with every other contours. Over-plotted are compact (< 2 pc) radio VLBI continuum sources (Varenius et al. 2017). (c) Imaged with `robust=-1`. The n -th contours are at $\pm 3n\sigma$ ($1 \leq n \leq 8$) and $3 \times 8(n-7)^{1.25}\sigma$ ($8 \leq n$), where $\sigma = 2.3$ K. The peak intensity is 57 K in Arp 220 E and 316 K in Arp 220 W.

6. FURTHER ANALYSIS AND DISCUSSION

6.1. Nuclear Disks and Outflow from Arp 220 W

We ascribe the larger components (E_2 and W_2) in our two-Gaussian (2G) model to the nuclear disks of Arp 220 that rotate around individual nuclei (Sakamoto et al. 1999). We attribute the elongation of these components on the sky to the disk inclinations and suggest that the faint feature perpendicular to the major axis of the western nuclear disk is a bipolar outflow.

The (counter-)rotating nuclear disks have been seen through velocity gradients along their major axes in high-resolution line imaging (Sakamoto et al. 1999, 2008; Scoville et al. 2015, 2017). If the disks are thin then their inclinations can be calculated from their axial ratios to be 60° for E_2 and 52° for W_2 , which agree with the estimates of BM15 for E_2' and W_2' . At least our inclination for the western nuclear disk is a lower limit because the outflow emission biases the measured axial ratio and the outflow-driving activity in the disk should give it a thickness. We thus estimate $i \approx 60^\circ$ for both disks. An apparent minor-to-major axis ratio of 0.62 for the western nuclear disk translates to an inclination in the range of $60^\circ \pm 10^\circ$ for an oblate spheroid having a height-to-radius ratio up to 0.55. On the western nuclear disk we therefore differ with S17 who, without seeing the faint bipolar component, modeled it as a thin face-on disk of $i \approx 30^\circ$. The CO velocity field in their Fig. 4 does suggest a nearly face-on configuration *if* the gas distribution is two-dimensional. However, a similar velocity field can be due to a three-dimensional bipolar outflow seen from the side (Seaquist & Clark 2001; Walter et al. 2002). Therefore, while it remains to be seen whether the CO data cube can be reasonably fitted with a three-dimensional outflow model, at least a projection of the cube (i.e., the mean velocity map) is consistent with a nearly edge-on outflow. The large inclination of the western nuclear disk explains the alignment of the supernova features (Fig. 4b'), which posed difficulty in S17's face-on disk model because any alignment at the time of star formation would be erased in the differentially-rotating disk by the time of supernova explosions. The large inclination of the western nuclear disk had been the preferred model since Scoville et al. (1998) inferred it from near infrared imaging with the Hubble Space Telescope.

Molecular outflow from individual nuclei of Arp 220, in particular from W, has been known from P-Cygni line profiles and blueshifted line absorption (Sakamoto et al. 2009; Rangwala et al. 2011; González-Alfonso et al. 2012; Veilleux et al. 2013; Tunnard et al. 2015; Martín et al. 2016; Barcos-Muñoz 2016; Zschaechner et al. 2016), which is also evident in the high resolution spectrum in Fig. 1 for the western nucleus. Sakamoto et al. (2009) also noted that OH masers observed by Rovilos et al. (2003) show a bipolar distribution around the western nucleus along its disk minor axis in the north-south direction, as one would expect for an outflow from the nuclear disk. Tunnard et al. (2015) proposed this to be the actual outflow configuration on the basis of their finding that SiO(6–5) at the systemic velocity is in absorption to the south and emission to the north of the nucleus. Varenus et al. (2016) further detected north-south extension of 150 MHz emission around the western nucleus at $\sim 0''.5$ resolution and attributed it to a bipolar outflow of the same configuration. Barcos-Muñoz (2016) found that a spectral index map between 33 and 92 GHz at $\sim 0''.08$ resolution has a distinct positive-value region across the western nuclear disk along P.A. $\sim 153^\circ$. Our observation of a bipolar structure in 3 mm continuum is consistent with these observations and corroborates the outflow from Arp 220 along P.A. $\sim 170^\circ$. Further evidence supporting this outflow will be presented in Barcos-Muñoz et al (in preparation).

In light of the revived picture of a highly inclined disk plus a bipolar outflow for the western nucleus, we notice that the CO maps of the nucleus in S17 (their Fig. 4) show a bipolar feature corresponding to that in the 3 mm continuum. Its southern part is more prominent and blueshifted. Tunnard et al. (2015) already proposed that the southern side of the bipolar outflow is approaching to us, i.e., blueshifted. For this velocity structure, the southern side of the western nuclear disk must be its far side if the outflow axis is normal to the disk. This is at odds with the near infrared observation that the southern side has much larger extinction and should be the near side of the nuclear disk (Scoville et al. 1998). Therefore, there remain unsolved problems about the detailed configuration of the outflow and the inner structure of the western nuclear disk. It may be that the outflow axis is not perpendicular to the disk but only in the plane containing the disk rotation axis and our sight line, or the disk may be warped. Regarding the outflow driver, both nuclear disks at least have vigorous star formation as traced by the VLBI supernovae. In addition, the core component W_1 , with its very high luminosity surface density (see §6.5), probably makes a large or even dominant contribution to drive the outflow. The outflow has oblique angles with respect to the major and minor axes of W_1 (and W_1') while it is orthogonal to the W_2 major axis. This implies a role of the nuclear disk for outflow collimation but, as noted above, three dimensional configuration of the system is necessary to verify this. On Arp

220 E, while blueshifted absorption was also detected toward it, the lack of a bipolar feature at 3 mm in this nucleus despite both nuclear disks apparently having large inclinations suggests that the outflow from the eastern nucleus has a less mass or a less 3 mm emissivity or both.

6.2. Fractional Contribution of Dust Emission

We estimate from spectral indices that the fractional contribution of dust emission to the 3 mm continuum is $f_d \approx 13\%$ and 41% for Arp 220 E and W, respectively. If dust emission with a spectral index α_d makes a fractional contribution f_d to the observed flux density and the rest of the emission from plasma, which is the sum of synchrotron and free-free emission, has a spectral index α_p then the total emission has a spectral index of $\alpha = f_d \alpha_d + (1 - f_d) \alpha_p$.⁴ We use $\alpha_d = 3.8$ for optically thin dust emission using the dust emissivity index β of 1.8 ± 0.1 in the Galactic plane (Planck Collaboration et al. 2011) and $\alpha_p = -0.59 \pm 0.08$ for E and -0.61 ± 0.07 for W from the 6–33 GHz measurements by BM15. With the overall 3 mm spectral indices that we estimated from Fig. 1, we obtain $f_d = 0.13 \pm 0.04$ and 0.41 ± 0.05 for Arp 220 E and W, respectively. The errors do not include the effect of any variation of the plasma spectral index between 6–33 GHz and ~ 100 GHz. Although α_p likely increases at higher frequencies as the fractional contribution of free-free emission increases, its effect to f_d should be small because BM15 found from cm-wave data that synchrotron emission dominates at 33 GHz (and attributed the weakness of free-free emission to dust absorption of ionizing photons). For example, if synchrotron emission has a constant spectral index -0.7 and free-free emission at -0.1 then the fractional contribution of synchrotron to the 33 GHz continuum having $\alpha = -0.6$ should be $5/6 = 83\%$. The synchrotron fraction decreases only slightly to 71% and α_p increases only slightly to -0.53 at 104 GHz. For this α_p the dust contribution to 3 mm continuum will decrease only by 0.01 for each nucleus. Likewise, if a part of the dust emission is saturated (i.e., opacity $\gtrsim 1$) at 3 mm or the dust β is smaller than assumed (e.g., median β is 1.6 in single-temperature fits for a sample of ULIRGs (Clements et al. 2010)) then f_d increases slightly, only by 0.01 for E and 0.03 for W for $\alpha_d = 3.5$. It is notable that for each nucleus the estimated fraction of dust emission broadly agrees with the flux-density fraction of the compact component in our 2G fit, 20% for E and 47% for W (§4.3).

One could also estimate dust emission by subtracting the plasma component from the observed total emission. Arp 220 E and W should have 104.1 GHz flux densities of 15.1 ± 2.3 and 16.4 ± 2.4 mJy, respectively, from synchrotron and free-free emission if we extrapolate the 33 GHz flux densities with the 6–33 GHz spectral indices in BM15. The errors include 12% absolute flux calibration uncertainty at 33 GHz. The ALMA total flux densities at the same frequency are estimated to be 11.9 ± 0.9 and 23.9 ± 1.3 mJy, for E and W respectively, from the 2G fit assuming a power-law among the nine frequency segments; the uncertainties include 5% error in absolute flux scale. Nominally, f_d is calculated from these flux densities to be -0.27 and 0.31 in Arp 220 E and W, respectively. The unphysical negative fraction may be simply because the denominator or numerator or both are in error; the fraction could be zero if both are in error by 1σ from the estimates above. Other possible sources for error include the flux calibration both at VLA and ALMA, missing flux in ALMA data that may be larger for a more extended eastern nucleus, and change in spectral index of the plasma emission between 33 and 100 GHz. Because the previous method to estimate f_d from the spectral indices alone is not affected by the first two of these errors, we adopt the f_d estimates in the previous paragraph. We note that S17, despite using this direct subtraction method, could obtain f_d of 0.11 and 0.45 respectively for E and W at 112.6 GHz. Our adopted estimates agree with theirs.

6.3. Distribution of Dust Emission in the Nuclei

We can estimate the spatial distribution of dust emission in the nuclei by subtracting plasma emission. For the latter emission we use the exponential disks that BM15 fitted to the Arp 220 nuclei at 33 GHz. We adopt their deconvolved shapes, place the plasma disks in our 1G fit positions, and scale the model flux densities to be consistent with the ALMA flux densities of the nuclei multiplied by their adopted $(1 - f_d)$. Within the 100 GHz band we assume that the plasma disks retain their 33 GHz spectral indices.

Figure 5 is a dust emission map made using all CDC₂ data. The dust emission in each nucleus has the strongest peak at the center and also has weaker peaks around it. The central concentration of the dust emission is much more

⁴ A spectrum that consists of power law spectra having spectral indices α_i and fractional contributions w_i at a reference frequency ν_0 ,

$$S_\nu = S_{\nu_0} \sum_i w_i \left(\frac{\nu}{\nu_0} \right)^{\alpha_i}, \quad \text{where } \sum_i w_i = 1,$$

has the spectral index

$$\alpha = \left. \frac{d \log S_\nu}{d \log \nu} \right|_{\nu=\nu_0} = \left[\frac{\nu}{S_\nu} \frac{d S_\nu}{d \nu} \right]_{\nu=\nu_0} = \sum_i w_i \alpha_i$$

at the reference frequency.

pronounced than that of the VLBI sources in both nuclei and in particular in the western nucleus. This compactness of dust emission compared to VLBI supernova distribution in Arp 220 W was already noted at 0.86 mm (Sakamoto et al. 2008). The central peak of 3 mm dust emission is much stronger in Arp 220 W than in Arp 220 E. This partly corresponds to the larger fractional contribution of dust emission in Arp 220 W ($\sim 41\%$ at 3 mm) than in Arp 220 E ($\sim 13\%$). The weaker peaks around the central ones may be dust emission from the nuclear disks but some of them can be residual plasma emission because we only subtracted its parametrized approximation. We also caution about an underlying assumption in this subtraction that all emission is optically thin. If the dust emission toward the center of a nucleus is optically thick then it is unnecessary to subtract plasma emission from behind the dust photosphere because such emission does not reach us in the first place. It is therefore possible that the dust emission peaks are more pronounced than seen in Fig. 5 at the centers of the two nuclei, in particular the western nucleus where the spectral index of W_1 is compatible with optically thick emission.

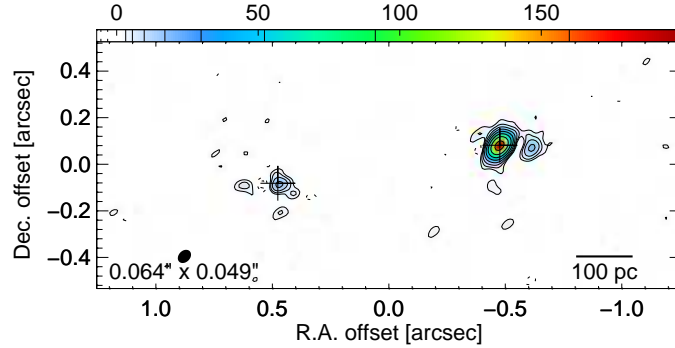


Figure 5. Arp 220 dust continuum emission at 104.1 GHz (2.9 mm). It is estimated by subtracting plasma emission in the forms of elliptical exponential disks measured at 33 GHz. This image was made with `robust=0` after the subtraction in the $u-v$ domain. The FWHM beam size is at the bottom-left corner. The offset coordinates are from the midpoint of the two nuclei. The crosses are at the continuum 1G-fit positions in Table 1. The n -th contour is at $\pm 3n^{1.75}\sigma$ where $\sigma = 1.06$ K ($30 \mu\text{Jy beam}^{-1}$). Negative contours are dashed. The peak intensity is 20 K in Arp 220 E and 199 K in Arp 220 W. The intensity unit of the color bar is kelvin (Rayleigh-Jeans brightness temperature).

We already obtained the parameters of the dust emission through the visibility fitting with the 1G+1E model (§4.4). In the fitting, the parameters of the model exponential disks were fixed to those of the plasma emission. The results for the Gaussian (dust) components are consistent with our image-domain estimate for dust emission regarding the presence of compact peaks at the centers of the two nuclei. The caution about the possible over-subtraction toward the center of the western nucleus applies to this visibility fitting too. The peak brightness temperature of the dust emission at the center of the western nucleus, $\gtrsim 500$ K, is more than twice higher than any previous measurements of dust brightness temperature in Arp 220. For example, Downes & Eckart (2007, ~ 90 K), Sakamoto et al. (2008, ~ 160 K), Wilson et al. (2014, ~ 200 K), and Scoville et al. (2017, ~ 120 K) all reported deconvolved peak brightness temperatures of dust continuum only up to 200 K with single-Gaussian deconvolved FWHM of $\sim 0''.1-0''.2$. There have been, however, pieces of spectroscopic evidence for much warmer dust and molecular gas in the galaxy (e.g., Martín et al. 2011; Rangwala et al. 2011; González-Alfonso et al. 2012, 2013).

6.4. Bolometric Luminosity of the Compact Core in the Western Nucleus

The bolometric luminosity of the compact core found in the western nucleus can be estimated as follows for its thermal dust emission. A geometrically-thin and optically-thick disk with a radial temperature described by a Gaussian falloff has a bolometric luminosity of

$$\begin{aligned}
 L_{\text{bol}} &= 2 \int_{-\infty}^{\infty} \int_{-\infty}^{\infty} \sigma \left[T_p \exp \left(-\log 2 \frac{x^2 + y^2}{r_{\text{maj}}^2} \right) \right]^4 dx dy \\
 &= \frac{\pi r_{\text{maj}}^2 \sigma T_p^4}{2 \log 2} \\
 &= 3.2 \times 10^9 \left(\frac{r_{\text{maj}}}{10 \text{ pc}} \right)^2 \left(\frac{T_p}{100 \text{ K}} \right)^4 L_{\odot},
 \end{aligned} \tag{1}$$

where the factor of 2 before the integral is for the two faces of the disk, σ is the Stefan-Boltzmann constant, T_p is the peak dust temperature, and r_{maj} is (major-axis FWHM)/2 of the Gaussian temperature distribution in linear scale. For W_1' , we obtain $L_{\text{bol}} = (3.3 \pm 0.8) \times 10^{12} L_{\odot}$ from $r_{\text{maj}} = 11.5 \pm 0.3$ pc and $T_p = 529 \pm 20$ K as well as 5% absolute flux-scale uncertainty. Here brightness temperature of the dust emission is equated with dust physical temperature. This L_{bol} is four times larger than the one for the western nucleus by [Wilson et al. \(2014\)](#), who used the same formula and 0.43 mm data ($T_p = 197$ K and $r_{\text{maj}} = 41$ pc scaled to our adopted distance), and is 1.7 times larger than the $L_{8-1000 \mu\text{m}}$ of Arp 220.

There are cautions for and limitations in the luminosity estimate and comparison above. First, our subtraction of plasma emission had an assumption that the dust (as well as plasma) emission is optically thin at 3 mm while the calculation above assumes an optically thick emitter. Even if the dust emission around the peak has a 3 mm opacity below unity it cannot be much below because dust cannot be hotter than its sublimation temperature; one obtains $\tau_{3\text{mm}} > 0.25$ from $\max(T_b)/\tau_{3\text{mm}} \approx T_{\text{dust}} < 2000$ K. The dust is therefore expected to become optically thick at shorter wavelengths not far from 3 mm because of the wavelength-dependent opacity coefficient. Observations at shorter wavelengths also suggest so ([Sakamoto et al. 2008](#); [Wilson et al. 2014](#)). In such a situation, the bolometric luminosity of the W_1' component can be higher than the calculation above because at shorter wavelengths where most of the luminosity is radiated the nucleus can radiate at a higher brightness temperature than at 3 mm, at T_{dust} instead of $(1 - e^{-\tau})T_{\text{dust}}$. To rectify, we can adopt an assumption that the 3 mm continuum toward the center of Arp 220 W is optically thick, which is consistent with the spectral index of W_1 in the 2G fit. Using the W_1 parameters, the bolometric luminosity of the core is calculated to be $(5.7 \pm 1.2) \times 10^{12} L_{\odot}$. Second, the total luminosity from Eq. (1) integrates direction-dependent radiation from the disk over the entire directions whereas the observational source luminosity $L_{8-1000 \mu\text{m}}$ is based on our measurements from a single direction and is calculated assuming isotropy. The latter luminosity can be biased for a disk-like source with anisotropic radiation. Most of the bolometric luminosity of Arp 220 is observed at mid-to-far infrared wavelengths around $50 \mu\text{m}$. Hence most of the luminosity from the 500 K core is absorbed and re-radiated before reaching us, presumably in large part by the nuclear disk W_2 . Because we look at W_2 (as well as E_2) from the side, i.e., from directions with less flux, $L_{8-1000 \mu\text{m}}$ of Arp 220 may well be underestimated. Third, we assumed that each nucleus is an axisymmetric disk to derive its inclination and luminosity, but this may not be valid. Removing the assumption, the lowest disk luminosity can be obtained by replacing r_{maj}^2 with $r_{\text{maj}}r_{\text{min}}$ in Eq. (1). It is $(1.9 \pm 0.5) \times 10^{12} L_{\odot}$ for W_1' , which agrees with the $L_{8-1000 \mu\text{m}}$ of Arp 220. This is the limiting case in which W_1' is an oval-shaped disk observed face-on. Fourth, the true distribution of brightness temperature in W_1 as well as W_1' may not be Gaussian and may be more flat-topped. Or it may be that the 33 GHz emission has a weak central cusp in addition to the exponential disk but it was missed in the observations at $0''.07$ resolution. If it were due to opaque free-free emission then it can become significant at 100 GHz. Because of the $\propto T^4$ dependence, L_{bol} in these cases would be smaller than the calculations above.

To summarize, the bolometric luminosity of the dust thermal emission from the central component in Arp 220 W is estimated to be $\sim 10^{12.5} L_{\odot}$ with at least ± 0.2 dex uncertainty due to various assumptions. It is as large as most of the bolometric luminosity of Arp 220 and may even exceed the $L_{8-1000 \mu\text{m}}$ of Arp 220 estimated from our vantage point. Higher resolution data will help improve the luminosity estimate by better constraining the shape and temperature of the core. More frequency coverage will also help to better extract dust thermal emission from the mixture of dust continuum, synchrotron, free-free, and line emission at millimeter and submillimeter wavelengths. In passing we add that the dust temperatures in E_1' and the two nuclear disks are very likely higher than their low brightness temperatures in 3 mm dust emission because dust is probably optically thin in these components. If so they may also have considerable luminosities that will be better constrained with observations at shorter wavelengths.

6.5. Luminosity Source and Evolution of the Western Nucleus

The high peak intensity of continuum emission at the center of Arp 220 W constrains the luminosity source, with the caveats in the preceding section. The peak brightness temperature of dust thermal emission, $T_p = 5.3 \times 10^2$ K for the W_1' component, translates to a peak luminosity surface density of $\sigma T_p^4 = 1.1 \times 10^{16} L_{\odot} \text{kpc}^{-2}$. Since we do not know fine details of the spatial distribution of the continuum emission, more robust than the peak values are the means in the half-light diameter (= FWHM for a Gaussian), namely the mean brightness temperature $\langle T_b \rangle_{1/2} = 3.8 \times 10^2$ K and mean luminosity surface density $\sigma(\langle T_b \rangle_{1/2})^4 = 3 \times 10^{15} L_{\odot} \text{kpc}^{-2}$ in the central 23 pc. For comparison, [Soifer et al. \(2003\)](#) obtained from mid-IR observations of three Seyfert nuclei the surface brightnesses of $(1 - 5) \times 10^{14} L_{\odot} \text{kpc}^{-2}$ at similar linear scales (10–30 pc). The surface brightnesses of infrared-luminous starburst galaxies and Galactic H II

regions are typically an order of magnitude (or more) below these Seyfert values (Soifer et al. 2001; Evans et al. 2003). Barcos-Muñoz et al. (2017) estimated luminosity surface densities in the 33 GHz half-light radii (30 pc to 1.7 kpc) for 22 local ultra/luminous infrared galaxies including those with AGNs. Their maximum value is $1 \times 10^{14} L_{\odot} \text{kpc}^{-2}$ and the mode is at $1 \times 10^{13} L_{\odot} \text{kpc}^{-2}$. This agrees with earlier analysis by Thompson et al. (2005) who not only showed statistics on IR luminous galaxies but derived $10^{13} L_{\odot} \text{kpc}^{-2}$ as a characteristic value for warm starbursts ($T < 200$ K) constrained by radiation pressure on dust. Soifer et al. (2003) noted that super star clusters (SSCs) can have as high a luminosity surface density at pc scale as the Seyfert nuclei do at a few 10 pc scale. For example, the most luminous SSC in the dwarf galaxy NGC 5253 has an age ~ 1 Myr, FWHM size ~ 1 pc, mass $\sim 10^{5.5} M_{\odot}$ (Turner & Beck 2004; Calzetti et al. 2015) and hence a luminosity $\sim 10^{8.5} L_{\odot}$ and luminosity surface density $\sim 10^{14.5} L_{\odot} \text{kpc}^{-2}$. The Arches cluster in the center of our Galaxy also has almost the same luminosity surface density (Lang et al. 2005). From this comparison, empirically speaking, a luminous AGN is a plausible source of luminosity for the central core $W_1 \approx W_1'$ in the western nucleus. Obviously, an empirical argument cannot rule out the possibility that by far the most intense starburst in the local universe is at the center of Arp 220 W. Our new constraint for the case where star formation dominates the luminosity is that the starburst in the central 20 pc must be equivalent to several thousands of massive young SSCs. Tighter constraints on the luminosity source are expected from further ALMA observations.

The center of Arp 220 W likely has a column density to make 3 mm dust opacity on the order of unity and hence a mass surface density of $\sim 10^6 M_{\odot} \text{pc}^{-2}$ (S17; BM15; and §6.4). The central 20 pc of Arp 220 W is therefore at or above the Eddington limit for dust (Andrews & Thompson 2011, see eq. (7)). The bipolar outflow from Arp 220 W is therefore expected. The nucleus has been actively forming stars in the nuclear disk, feeding either a luminous AGN or exceptionally intense starburst at the center, and blowing out dust and gas at the same time. The nucleus is certainly in a phase of rapid evolution.

7. CONCLUSIONS

We have analyzed ALMA high-resolution data of Arp 220 at ~ 3 mm wavelengths. We spatially resolved continuum structure of the individual nuclei and decomposed the nuclei to plasma and dust emission. The dust emission was then used to characterize the luminosity source in the western nucleus. Our major observations are the following.

1. Both nuclei are found to have at least two structural components at 3 mm. Two concentric components such as Gaussians or a Gaussian and an exponential disk provide reasonable fits to the observed visibilities.
2. The larger components in the two-Gaussian fit have FWHM sizes $\sim 0''.23$ – $0''.37$ (100–150 pc) and axial ratios ~ 2 . They match in shape and extent the distributions of supernova features seen with VLBI. We identify them to the starburst nuclear disks rotating around individual nuclei with inclinations $\approx 60^\circ$.
3. The smaller components in the two-Gaussian fit contribute about 20% and 50% of the 3 mm continuum flux densities of the eastern and western nuclei, respectively. They have FWHM sizes of 20–40 pc and peak brightness temperatures 70–640 K, which are more than twice smaller and brighter than in the previous single-Gaussian fit of the same data.
4. The 3 mm continuum spectral slopes are flat ($S_{\nu} \propto \nu^{0.0 \pm 0.2}$) and positive ($\propto \nu^{1.2 \pm 0.2}$) at the eastern and western nuclei, respectively. Combining them with 33 GHz data of plasma emission, we estimate that dust emits about 13% and 41% of the 3 mm continuum in the eastern and western nuclei, respectively. The dust emission is found centrally concentrated in both nuclei. These central cores of dust emission correspond to the compact components in our two-component fitting.
5. The dust-continuum core of the western nucleus is estimated to have a peak brightness temperature of ~ 530 K and major axis FWHM of about 20 pc after subtracting plasma emission. Assuming a dust disk, its bolometric luminosity can be as large as $\sim 10^{12.5} L_{\odot}$ or at least a large fraction of the total luminosity of Arp 220. Its luminosity surface density is on the order of $10^{15.5} L_{\odot} \text{kpc}^{-2}$ in 20 pc scale. This is about an order of magnitude higher than observed toward Seyfert nuclei at the same scale and super-star clusters at pc scale. This comparison favors the presence of a luminous AGN on empirical grounds, but we stress the uncertainties still in the data interpretation, the inherent limitation of the empirical argument, and the need for further observational and theoretical constraints.
6. The western nucleus has a faint extended, linear feature along the projected minor axis of its nuclear disk; this is the third structural component for the nucleus. We attribute it to the previously inferred bipolar outflow.

We are grateful to the ALMA Observatory and its data archive team for the observations and data we used here. We thank the ALMA help desk for their prompt response to our numerous inquiries about ALMA observations and data reduction. We also thank our referee for comments that helped clarify this paper. This paper makes use of the following ALMA data: ADS/JAO.ALMA#2015.1.00113.S and ADS/JAO.ALMA#2011.0.00001.CAL. ALMA is a partnership of ESO (representing its member states), NSF (USA) and NINS (Japan), together with NRC (Canada), MOST and ASIAA (Taiwan), and KASI (Republic of Korea), in cooperation with the Republic of Chile. The Joint ALMA Observatory is operated by ESO, AUI/NRAO and NAOJ. This research has made use of NASA’s Astrophysics Data System Bibliographic Services. This research has also made use of the NASA/IPAC Extragalactic Database (NED), which is operated by the Jet Propulsion Laboratory, California Institute of Technology, under contract with the National Aeronautics and Space Administration. KS is supported by MOST grants 105-2119-M-001-036 and 106-2119-M-001-025.

Facility: ALMA

Software: CASA v4.7.2 (McMullin et al. 2007), mpfit (Moré 1977; Moré & Wright 1993; Markwardt 2009)

REFERENCES

- Aladro, R., Martín, S., Riquelme, D., et al. 2015, *A&A*, 579, A101
- Andrews, B. H., & Thompson, T. A. 2011, *ApJ*, 727, 97
- Armus, L., Mazzarella, J. M., Evans, A. S., et al. 2009, *PASP*, 121, 559
- Barcos-Muñoz, L., Leroy, A. K., Evans, A. S., et al. 2015, *ApJ*, 799, 10
- Barcos-Muñoz, L., 2016, Ph. D. Thesis, University of Virginia
- Barcos-Muñoz, L., Leroy, A. K., Evans, A. S., et al. 2017, *ApJ*, 843, 117
- Batejat, F., Conway, J. E., Hurley, R., et al. 2011, *ApJ*, 740, 95
- Briggs, D. S. 1995, Ph. D. thesis, New Mexico Institute of Mining and Technology
- Calzetti, D., Johnson, K. E., Adamo, A., et al. 2015, *ApJ*, 811, 75
- Cicone, C., Maiolino, R., Sturm, E., et al. 2014, *A&A*, 562, A21
- Clements, D. L., Dunne, L., & Eales, S. 2010, *MNRAS*, 403, 274
- Downes, D., & Eckart, A. 2007, *A&A*, 468, L57
- Evans, A. S., Becklin, E. E., Scoville, N. Z., et al. 2003, *AJ*, 125, 2341
- Genzel, R., Tacconi, L. J., Rigopoulou, D., Lutz, D., & Tecza, M. 2001, *ApJ*, 563, 527
- González-Alfonso, E., Fischer, J., Graciá-Carpio, J., et al. 2012, *A&A*, 541, A4
- González-Alfonso, E., Fischer, J., Bruderer, S., et al. 2013, *A&A*, 550, A25
- Hopkins, P. F., Hernquist, L., Cox, T. J., & Kereš, D. 2008, *ApJS*, 175, 356-389
- Lang, C. C., Johnson, K. E., Goss, W. M., & Rodríguez, L. F. 2005, *AJ*, 130, 2185
- Lonsdale, C. J., Diamond, P. J., Thrall, H., Smith, H. E., & Lonsdale, C. J. 2006, *ApJ*, 647, 185
- Markwardt, C. B. 2009, *Astronomical Data Analysis Software and Systems XVIII*, 411, 251
- Martín, S., Krips, M., Martín-Pintado, J., et al. 2011, *A&A*, 527, A36
- Martín, S., Aalto, S., Sakamoto, K., et al. 2016, *A&A*, 590, A25
- Martí-Vidal, I., Pérez-Torres, M. A., & Lobanov, A. P. 2012, *A&A*, 541, A135
- McMullin, J. P., Waters, B., Schiebel, D., Young, W., & Golap, K. 2007, *Astronomical Data Analysis Software and Systems XVI*, 376, 127
- Moré, J. 1977, “The Levenberg-Marquardt Algorithm: Implementation and Theory,” in *Numerical Analysis*, vol. 630, ed. G. A. Watson (Springer-Verlag: Berlin), 105
- Moré, J. & Wright, S. 1993, *Optimization Software Guide*, *Frontiers in Applied Mathematics*, vol. 14, (Philadelphia, PA: SIAM)
- Paggi, A., Fabbiano, G., Risaliti, G., et al. 2017, *ApJ*, 841, 44
- Parra, R., Conway, J. E., Diamond, P. J., et al. 2007, *ApJ*, 659, 314
- Planck Collaboration, Abergel, A., Ade, P. A. R., et al. 2011, *A&A*, 536, A21
- Rangwala, N., Maloney, P. R., Glenn, J., et al. 2011, *ApJ*, 743, 94
- Rovilos, E., Diamond, P. J., Lonsdale, C. J., Lonsdale, C. J., & Smith, H. E. 2003, *MNRAS*, 342, 373

- Sakamoto, K., Scoville, N. Z., Yun, M. S., et al. 1999, *ApJ*, 514, 68
- Sakamoto, K., Wang, J., Wiedner, M. C., et al. 2008, *ApJ*, 684, 957-977
- Sakamoto, K., Aalto, S., Wilner, D. J., et al. 2009, *ApJL*, 700, L104
- Sakamoto, K., Aalto, S., Costagliola, F., et al. 2013, *ApJ*, 764, 42
- Sakamoto, K., Aalto, S., Combes, F., Evans, A., & Peck, A. 2014, *ApJ*, 797, 90
- Sanders, D. B., & Mirabel, I. F. 1996, *ARA&A*, 34, 749
- Scoville, N. Z., Evans, A. S., Dinshaw, N., et al. 1998, *ApJL*, 492, L107
- Scoville, N., Sheth, K., Walter, F., et al. 2015, *ApJ*, 800, 70
- Scoville, N., Murchikova, L., Walter, F., et al. 2017, *ApJ*, 836, 66
- Seaquist, E. R., & Clark, J. 2001, *ApJ*, 552, 133
- Smith, H. E., Lonsdale, C. J., Lonsdale, C. J., & Diamond, P. J. 1998, *ApJL*, 493, L17
- Soifer, B. T., Neugebauer, G., Matthews, K., et al. 2001, *AJ*, 122, 1213
- Soifer, B. T., Bock, J. J., Marsh, K., et al. 2003, *AJ*, 126, 143
- Thompson, T. A., Quataert, E., & Murray, N. 2005, *ApJ*, 630, 167
- Turner, J. L., & Beck, S. C. 2004, *ApJL*, 602, L85
- Tunnard, R., Greve, T. R., Garcia-Burillo, S., et al. 2015, *ApJ*, 800, 25
- Varenius, E., Conway, J. E., Martí-Vidal, I., et al. 2016, *A&A*, 593, A86
- Varenius, E., Conway, J. E., Batejat, F., et al. 2017, *arXiv:1702.04772*
- Veilleux, S., Meléndez, M., Sturm, E., et al. 2013, *ApJ*, 776, 27
- Walter, F., Weiss, A., & Scoville, N. 2002, *ApJL*, 580, L21
- Wiedner, M. C., Wilson, C. D., Harrison, A., et al. 2002, *ApJ*, 581, 229
- Wilson, C. D., Rangwala, N., Glenn, J., et al. 2014, *ApJL*, 789, L36
- Yoast-Hull, T. M., Gallagher, J. S., Aalto, S., & Varenius, E. 2017, *MNRAS*, 469, 89
- Zschaechner, L. K., Ott, J., Walter, F., et al. 2016, *ApJ*, 833, 41